Revised, 10/XX/2024

# Elucidating the Intrinsic Relationship between Redox Properties of $CeO_2$ and $CH_4$ Oxidation Activity: A Theoretical Perspective

Juan Li [1], Shuyun Zhou [1], Peng Li [1], Shulan Zhou [3], Qiang Wan [1,4], Hua Guo [5], and Sen Lin [1,2,a)]

[1] State Key Laboratory of Photocatalysis on Energy and Environment, College of Chemistry, Fuzhou University; Fuzhou, 350002, China

[2] Fujian Provincial Key Laboratory of Theoretical and Computational Chemistry, Xiamen 361005, China

[3] School of Chemistry and Chemical Engineering, Shandong University of Technology, Zibo 255049, Shandong, China

[4] Key Laboratory of the Ministry of Education for Advanced Catalysis Materials, Institute of Physical Chemistry, Zhejiang Normal University, Jinhua, 321004, China

[5] Department of Chemistry and Chemical Biology, Center for Computational Chemistry, University of New Mexico, Albuquerque, New Mexico, 87131, USA

a) Author to whom correspondence should be addressed: slin@fzu.edu.cn

**ABSTRACT:** Methane ($CH_4$) oxidation is an important reaction to reduce the greenhouse effect caused by incomplete combustion of $CH_4$. Here, we explored the mechanism of $CH_4$ oxidation catalyzed by $CeO_2$ and Ni-doped $CeO_2$, focusing on the redox properties of these catalyst surfaces, using density functional theory (DFT). We found that the barriers for $CH_4$* activation and $H_2O$* formation are correlated with the surface redox capacity, which is enhanced by Ni doping. Furthermore, the complete reaction mechanism is explored by DFT calculations and microkinetic simulations on bare and Ni-doped $CeO_2$ surfaces. Our calculations suggest that the doping of Ni leads to a much higher overall reactivity, due to a balance between the $CH_4$* activation and $H_2O$* formation steps. These results provide insights into the $CH_4$ oxidation mechanism and the intrinsic relationship between redox properties and the activity of $CeO_2$ surfaces.

**Keywords**: DFT; Reaction mechanism; $CeO_2$; $CH_4$ oxidation; Microkinetic simulation

**Graphical abstract**

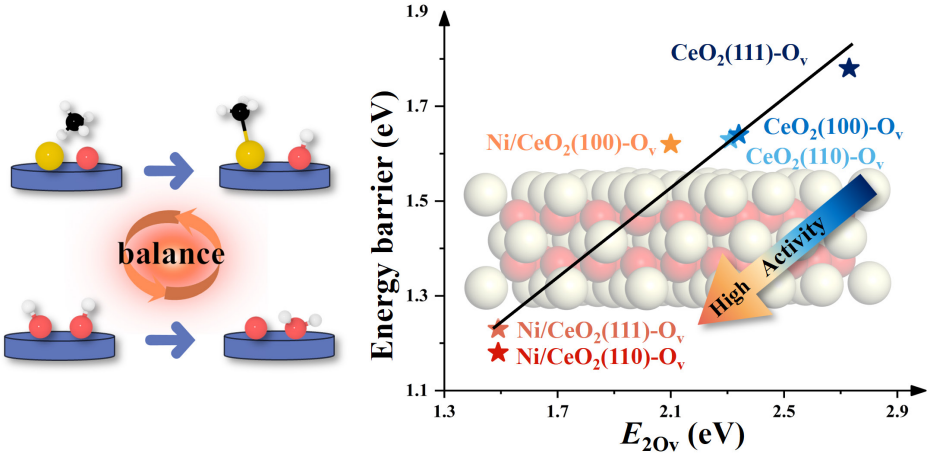

## I. INTRODUCTION

Natural gas, which is primarily composed of methane ($CH_4$), is considered as a much cleaner energy source than other fossil fuels due to its high H: C ratio. However, with the widespread use of natural gas engines, incomplete combustion of $CH_4$ could result in its escape to the atmosphere.[1] As a greenhouse gas twenty-five times more potent than $CO_2$, $CH_4$ oxidation towards the less harmful $CO_2$ is regarded as a practicable solution for reducing the greenhouse effect and has garnered much recent attention.[2-5] Since the complete conversion of $CH_4$ to $CO_2$ and $H_2O$ is difficult due to the strong C–H bond,[6] it is desirable to uncover the structure-activity relationship in order to design catalysts that are capable of effectively $CH_4$ oxidation at relatively low exhaust gas temperatures.

Noble metal and metal oxide-based catalysts are commonly used in catalyzing $CH_4$ oxidation. For example, Pt and Pd exhibit high affinities for $CH_4$ adsorption, leading to the efficient activation of C–H bonds.[7, 8] Huang et al.[9] for example, prepared a Pd-$NiCo_2O_4/SiO_2$ catalyst that achieved a 100% $CH_4$ conversion rate at 378 °C under lean $CH_4$ conditions. However, catalysts based on noble metals are known to have poor water tolerance, making them susceptible to deactivation in steam environments.[3] Ceria ($CeO_2$) is an alternative candidate for catalytic oxidation of $CH_4$ due to its reversible oxygen storage properties and the abundant $Ce^{4+}/Ce^{3+}$ pairs. Its hydrothermal stability in the presence of $H_2O$ is also noteworthy.[10, 11] There is ample evidence that the ability of the $CeO_2$ surface to store and release oxygen is closely related to the activity of catalytic oxidation reactions.[12-16] Su et al.[17] reported that Pd doping of $CeO_2$ surfaces

formed two $Pd^{2+}$ cations replacing a $Ce^{4+}$ cation. This led to stronger $CH_4$ adsorption and more reactive surface oxygens, ultimately reducing the $CH_4$ dissociation energy barrier and promoting oxygen vacancy recovery. More recently, Chen et al.[18] synthesized $CeO_2$-based catalysts with different morphologies, including nanoparticles, cubes, and rods, for catalyzing the complete oxidation of $CH_4$. The $CH_4$ oxidation activity of these catalysts was found to be closely related to their intrinsic redox properties, as demonstrated by $H_2$ temperature-programmed reduction and oxygen storage capacity measurements. Furthermore, the activity was greatly enhanced by Ni doping. Other studies also suggested that the introduction of dopants such as Rh, Pd, Pt, and Au into $CeO_2$ can increase the concentration of oxygen vacancies and the amount of active oxygen species in the respective morphologies of $CeO_2$, thereby promoting the reaction activity.[19, 20]

However, the detailed mechanism for $CH_4$ oxidation, in particular, the role of surface oxygen in $CH_4$ oxidation on $CeO_2$ surfaces and its impact on the overall catalytic performance remains obscure. Due to the high stability of the $CH_4$ molecule, its activation is often considered to be crucial for evaluating the activity of $CH_4$ conversion reactions, while vacancy formation energy is commonly used to describe the C–H activation properties.[21-23] On the other hand, the formation of the final product, $H_2O$, is also closely related to the surface redox properties. Previous studies have shown that the formation barrier of $H_2O$ on the pristine $CeO_2$(111) surface can be as high as 3.54 eV.[24] By doping metals, the stability of lattice oxygen can be reduced, facilitating the conversion of oxygen to $H_2O$, which significantly enhances the activity of $H_2$

oxidation and $CH_2O$ combustion reactions.[24, 25] Recently, Jung et al. reported a model of solid oxide fuel cells constructed with Sm-doped $CeO_{2-\delta}$ thin films.[26] The electrochemical impedance spectra and in situ XPS confirmed that the $H_2O$ formation step, rather than C–H cleava ge or $CO_2$ formation, limits the overall reaction rate in the $CH_4$ electrooxidation process. Mechanistic studies also suggested that the formation of $H_2O$ is the rate-determining step in the complete oxidation of $CH_4$ in $Ni/CeO_2$ and $MgAl_2O_4$ systems.[27, 28] Hence, it is important to investigate both reaction steps in assessing the catalytic activity of $CeO_2$ catalysts for $CH_4$ oxidation.

In our previous research, we reported a significant reduction of the energy required for oxygen vacancy formation upon Ni doping of $CeO_2$(111)/(110),[29, 30] which suggests a potential link between the surface redox properties and catalytic capacity of $CeO_2$ surfaces. In this work, we systemically investigate the three most stable surfaces of $CeO_2$ ($CeO_2$(111), (110), and (100)), along with their corresponding Ni-doped surfaces. This study is particularly relevant in light of the recent experimental work on the Ni-dopped $CeO_2$ catalysis of $CH_4$ oxidation.[18] Our study emphasizes the importance of a comprehensive assessment of the key steps of the activation of $CH_4$* and the formation of $H_2O$*. The analysis of surface properties and kinetics elucidates the fundamental reasons behind the enhancement of $CH_4$ oxidation activity facilitated by improved surface redox properties. Through DFT calculations and microkinetic simulations, we explored the complete reaction pathway and kinetics of $CH_4$ oxidation on both $CeO_2$ and Ni-doped $CeO_2$ surfaces. Our findings suggest that Ni doping modifies the surface properties of $CeO_2$, which in turn balances the energy barriers of the two key steps, thus

enhancing the overall reaction activity. This work provides new insights for the rational design of oxide catalysts for low-temperature $CH_4$ oxidation.

## II. COMPUTATIONAL DETAILS

### A. Methods

Spin-polarized DFT calculations were performed using the Vienna Ab initio Simulation Package (VASP) with the projector-augmented wave (PAW) treatment of the core electrons, while a plane-wave kinetic energy cutoff of 400 eV was applied to treat valence electrons.[31-33] The Perdew–Burke–Ernzerhof (PBE) functional with the generalized gradient approximation (GGA) was employed for the exchange-correlation potential and van der Waals dispersion forces between the adsorbate and surface were accounted for using the zero damping DFT-D3 method of Grimme.[34, 35] The DFT + $U$ approach with a $U$ value of 4.5 eV was utilized to address the strong on-site Coulomb and exchange interaction of localized Ce 4$f$ electrons.[36] Structural optimizations utilized a 3 × 3 × 1 $k$-point grid in the Monkhorst-Pack scheme, while electronic structure calculations employed a 5 × 5 × 1 $k$-point mesh.[37] Convergence criteria for force and energy were set to 0.05 eV/Å and $10^{-4}$ eV, respectively.

The climbing image-nudged elastic band (CI-NEB) method and the dimer approach were employed to locate the saddle points.[38, 39] The reaction energy ($\Delta E$) for an elementary step was determined by the energy difference between the initial state (IS) and its corresponding final state (FS). The activation barrier ($E_a$) was identified as the energy difference between the transition state (TS) and its corresponding initial state.

The formation energies of oxygen vacancies were calculated using the following equations: $E_{O_v} = E_{surface-O_v} - E_{surface} + 1/2E_{O_2}$ and $E_{2O_v} = E_{surface-2O_v} - E_{surface-O_v} + 1/2E_{O_2}$. Here, $E_{surface}$ represents the energy of the clean surface, $E_{surface-O_v}$ the energy of the surface with an oxygen vacancy, $E_{surface-2O_v}$ the energy of the surface with two oxygen vacancies and $E_{O_2}$ the energy of a gas-phase $O_2$ molecule.

Microkinetic simulations were conducted employing the CATKINAS package[40, 41] under experimental conditions[18] spanning temperatures from 400 to 1000 K and pressures from 0.01 to 1 bar. The feed ratio utilized was $CH_4$:$O_2$:Ar = 1:5:9, with a total flow rate of 30 sccm. The elementary reactions employed for the microkinetic simulations are enumerated in Table S1. In the microkinetic analysis, entropic (S) effects and zero-point energies (ZPE) were considered to estimate the Gibbs free energy change ($\Delta G$) of each elementary step, calculated as $\Delta G = \Delta H - T\Delta S + \Delta$ZPE.

## B. Models

The DFT optimized lattice parameter of bulk $CeO_2$ is 5.42 Å, which closely matches the experimental value of 5.41 Å.[42] Three crystal facets, namely (111), (110) and (100), were chosen for investigation in this study. For the $CeO_2$(111) surface, a 3×3 nine-layer slab comprising 27 Ce atoms and 54 O atoms was utilized. The bottom three layers of the slab were kept fixed. Similarly, the $CeO_2$(110) surface was modeled with a 2×3 five-layer slab containing 30 Ce atoms and 60 O atoms, with the bottom two layers fixed. For $CeO_2$(100), the surface instability is susceptible to reconstruction due to a dipole moment perpendicular to the surface. Therefore, we moved half of the

oxygen atoms in the top layer of the model to the opposite surface to eliminate the dipole, a method has been applied in previous studies.[43-45] Accordingly, a 2 × 2 seven-layer $CeO_2$(100) slab consisting of 24 Ce atoms and 48 O atoms was used, with its bottom two layers fixed. A vacuum space of 15 Å was set along the *z*-direction to avoid interactions between periodic images. Furthermore, Ni/$CeO_2$(111), Ni/$CeO_2$(110), and Ni/$CeO_2$(100) surfaces were obtained by replacing a surface Ce atom with a Ni atom with Ni doping mass fractions of 1.29, 1.16, and 1.46 wt %, respectively, which are close to the experimental measurement.[29]

## III. RESULTS ANS DISCUSSION

### A. Structures and properties for pristine and Ni-doped $CeO_2$ surfaces

Models of the Ni-doped $CeO_2$ surfaces were obtained by replacing Ce at different layers by Ni. Fig. 1 shows the lowest energy optimized geometries of the pristine $CeO_2$ and Ni-doped $CeO_2$ surfaces, denoted as $CeO_2$(111), $CeO_2$(110), $CeO_2$(100), Ni/$CeO_2$(111), Ni/$CeO_2$(110), and Ni/$CeO_2$(100), respectively. These favorable structures are all attributable to doping near the surface layer, with doping energies of 0.71, –0.25, and –0.58 eV, respectively (Table S2). Several other higher energies doping structures have been found as shown in Fig. S1, but they are not used in the mechanistic studies discussed below. As shown in Fig. 1, the introduction of Ni causes significant distortions on the $CeO_2$(111) and $CeO_2$(110) surfaces. To maintain structural stability, the Ni atom migrates downward and coordinates with four neighboring oxygens, forming a stable square planar structure. This motif suggests that the Ni is stable and

unlikely to participate in catalysis directly, as confirmed by DFT results discussed below. The two surface oxygens that were originally bonded to the replaced Ce are transformed into a two-coordinated configuration that bonded to two neighboring Ce atoms. As shown below, these oxygens are labile and involved in the catalysis. However, Ni doping does not change the surface lattice on $CeO_2$(100), with the Ni coordinated with four oxygen atoms, but not at a square planar geometry.

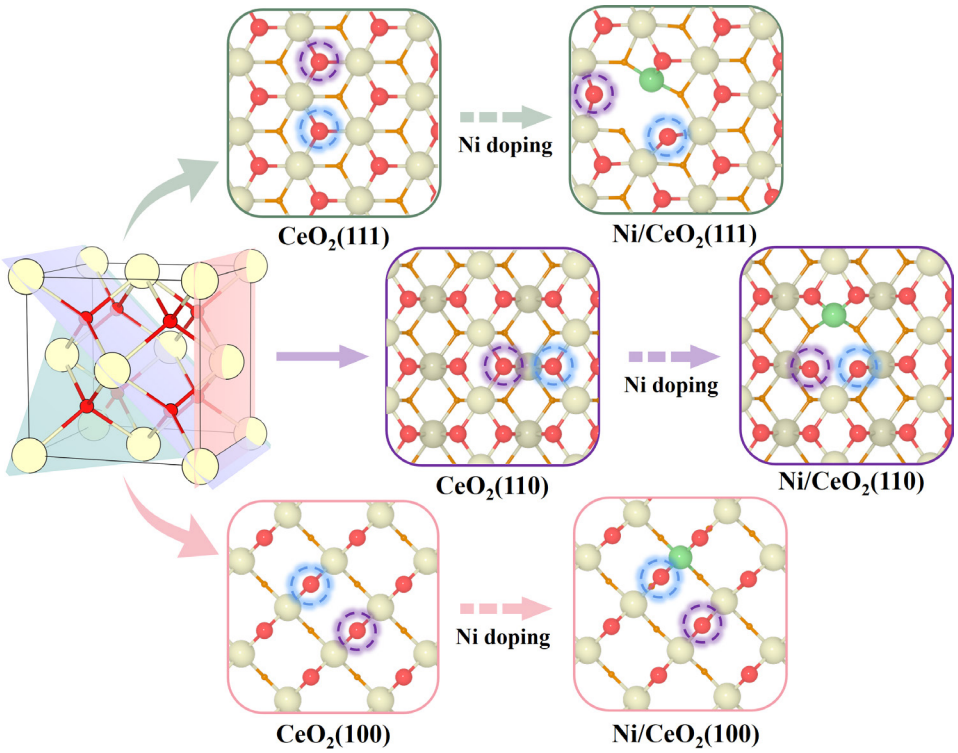


**FIG. 1.** Top view of optimized structures of pristine $CeO_2$ and Ni-doped $CeO_2$ surfaces. The dashed blue and purple circles represent locations of the first and second oxygen vacancies. Color scheme: Ce, yellow; Ni, green; surface O, red; subsurface O, orange. The (111), (110) and (100) facets of $CeO_2$ are color coded as green, violet and pink, respectively.

As discussed earlier, the catalytic activity of $CeO_2$-based catalysts for $CH_4$

oxidation is known to be strongly affected by their redox properties, which are related to the ease of surface oxygen vacancy formation. Therefore, we first investigated the formation of oxygen vacancy on $CeO_2$ and Ni/$CeO_2$ surfaces and named it as the first oxygen vacancy ($O_v$). The location of the first oxygen vacancy is indicated by the dashed blue circles in Fig. 1. The calculated lowest formation energy ($E_{Ov}$) of the first oxygen vacancy on pristine and Ni-doped $CeO_2$ surfaces is listed in Table 1. On pristine $CeO_2$, $E_{Ov}$ follows the order as (111) > (100) > (110), with $CeO_2$(110) having the lowest value of 1.73 eV, which is consistent with the previous conclusion by Wu et al.[46] Ni doping effectively promotes defect formation, especially on $CeO_2$(111) and $CeO_2$(110). The first oxygen vacancy formation on the Ni/$CeO_2$(111) and (110) surfaces is actually exothermic, with $E_{Ov}$ of –0.42 and –0.59 eV, respectively. This was also mentioned in our earlier papers.[29, 30] In comparison, the reduction of $E_{Ov}$ of $CeO_2$(100) is more modest, decreasing from 1.90 to 0.41 eV. Due to the easy formation of $O_v$ on Ni-doped $CeO_2$ surfaces, models with one $O_v$ (Ni/$CeO_2$-$O_v$) were used to simulate the $CH_4$ oxidation. To allow comparison with Ni/$CeO_2$-$O_v$, we also utilized the models with a single $O_v$ (denoted as $CeO_2$-$O_v$) for undoped $CeO_2$.

**TABEL 1.** The formation energy of the first ($E_{Ov}$) and second ($E_{2Ov}$) oxygen vacancies on the $CeO_2$ and Ni/$CeO_2$ surfaces.

| Surface | $E_{Ov}$ (eV) | $E_{2Ov}$ (eV) | Surface | $E_{Ov}$ (eV) | $E_{2Ov}$(eV) |
|---|---|---|---|---|---|
| $CeO_2$(111) | 2.57 | 2.73 | Ni/$CeO_2$(111) | –0.42 | 1.49 |
| $CeO_2$(110) | 1.73 | 2.31 | Ni/$CeO_2$(110) | –0.59 | 1.49 |

| | | | | | |
|---|---|---|---|---|---|
| $CeO_2(100)$ | 1.90 | 2.34 | $Ni/CeO_2(100)$ | 0.41 | 2.10 |

## B. Methane activation and water formation on $CeO_2$-$O_v$ and $Ni/CeO_2$-$O_v$ surfaces

Activation of $CH_4$ has often been considered the most crucial elementary step in the $CH_4$ conversion reactions.[21, 47] However, the formation of $H_2O$ is closely related to oxygen release and has recently been noted to play a key role in $CH_4$ oxidation.[24, 25] Therefore, we first focused on the energetics of the $CH_4$* activation and $H_2O$* formation steps on the $CeO_2$-$O_v$ and $Ni/CeO_2$-$O_v$ surfaces.

Metal cations with strong Lewis acidity and oxygen anions with strong Lewis basicity are known to be active in C–H bond cleavage.[48] Frustrated Lewis Pairs (FLPs), with a suitable spatial blockage between acidic sites and basic sites,[49, 50] have capacity to activate the $CH_4$ molecules.[51] In Fig. 2, the electron density isosurface displays the electrostatic potential distribution of the $CeO_2$-$O_v$ and $Ni/CeO_2$-$O_v$ surfaces. The exposed surface Ce atoms can form a Ce-O(a) FLP with non-adjacent oxygen atoms, which might serve as active sites for $CH_4$ activation. Our initial investigation is focused on the breakage of the first C–H bond by these FLP sites. To this end, $CH_4$ first adsorbs at the FLP site, followed by the breaking of the first C–H bond resulting in the adsorption of $CH_3$* and H* on the Ce cation and lattice oxygen sites, respectively. The corresponding geometries and energy barriers are shown in Fig. S2 and Table 2, respectively.

Table 2 and Fig. 3(a) show that for the $CeO_2$-$O_v$ surfaces, the (100) surface has the

most effective activation of the C–H bond, with an energy barrier of 0.78 eV. The (111) and (110) surfaces have higher energy barriers of 1.19 and 1.03 eV, respectively. These reactions are all endothermic. For the Ni/$CeO_2$-$O_v$ surfaces, the energy barrier for C–H bond breaking on the (100) surface has the lowest value at 1.07 eV. On the (111) surface, this step requires an energy barrier of 1.23 eV. On the (110) surface, the reaction has no barrier but with an endothermicity of 1.25 eV. This suggests that the ability of FLP sites for C–H bond breaking was weakened after Ni doping. This may be due to the less negative Bader charge values of the O(a) after Ni doping (Fig. 2), e.g., from –1.22|e| to –1.15|e| on the (111) surface, which reduces the ability of O(a) for accepting the hydridic H*. We also tried to calculate the C–H activation by the H abstraction mechanism, however the unstable $CH_3$• still returns to the surface to $CH_3$* during the optimization process. However, the above results seems to conflict with the positive correlation between surface redox properties and catalytic activity of $CeO_2$ observed in a previous experiment.[18]

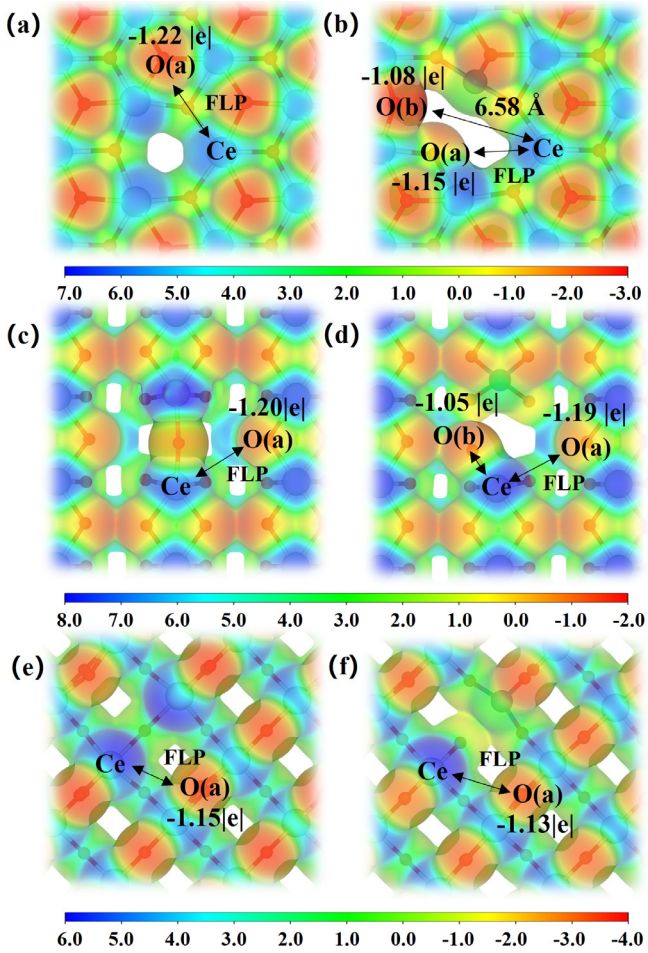


**FIG. 2.** Electron density isosurfaces of (a) $CeO_2(111)$-$O_v$, (b) $Ni/CeO_2(111)$-$O_v$, (c) $CeO_2(110)$-$O_v$, (d) $Ni/CeO_2(110)$-$O_v$, (e) $CeO_2(100)$-$O_v$ and (f) $Ni/CeO_2(100)$-$O_v$. The electron-density isosurfaces are plotted at 0.01 *e* $bohr^{-3}$. The color bar represents the electrostatic potential scale. The black numbers are the calculated Bader charge values. The Ce-O FLP sites are marked with arrows.

**TABLE 2.** Energy barriers for $CH_4$* activation ($E_{a1}$) and $H_2O$* formation ($E_{a2}$) on the $CeO_2$-$O_v$ and $Ni/CeO_2$-$O_v$ Surfaces.

| Surface | $E_{a1}$ (eV) | $E_{a2}$ (eV) | Surface | $E_{a1}$ (eV) | $E_{a2}$ (eV) |
|---|---|---|---|---|---|
| $CeO_2(111)$ | 1.19 | 1.78 | $Ni/CeO_2(111)$ | 1.23 | 0.83 |
| $CeO_2(110)$ | 1.03 | 1.62 | $Ni/CeO_2(110)$ | 1.25/1.18 | 1.06 |
| $CeO_2(100)$ | 0.78 | 1.64 | $Ni/CeO_2(100)$ | 1.07 | 1.63 |

Note: The numbers of 1.78, 1.64, and 1.25 eV are $\Delta E$ values without a transition state.

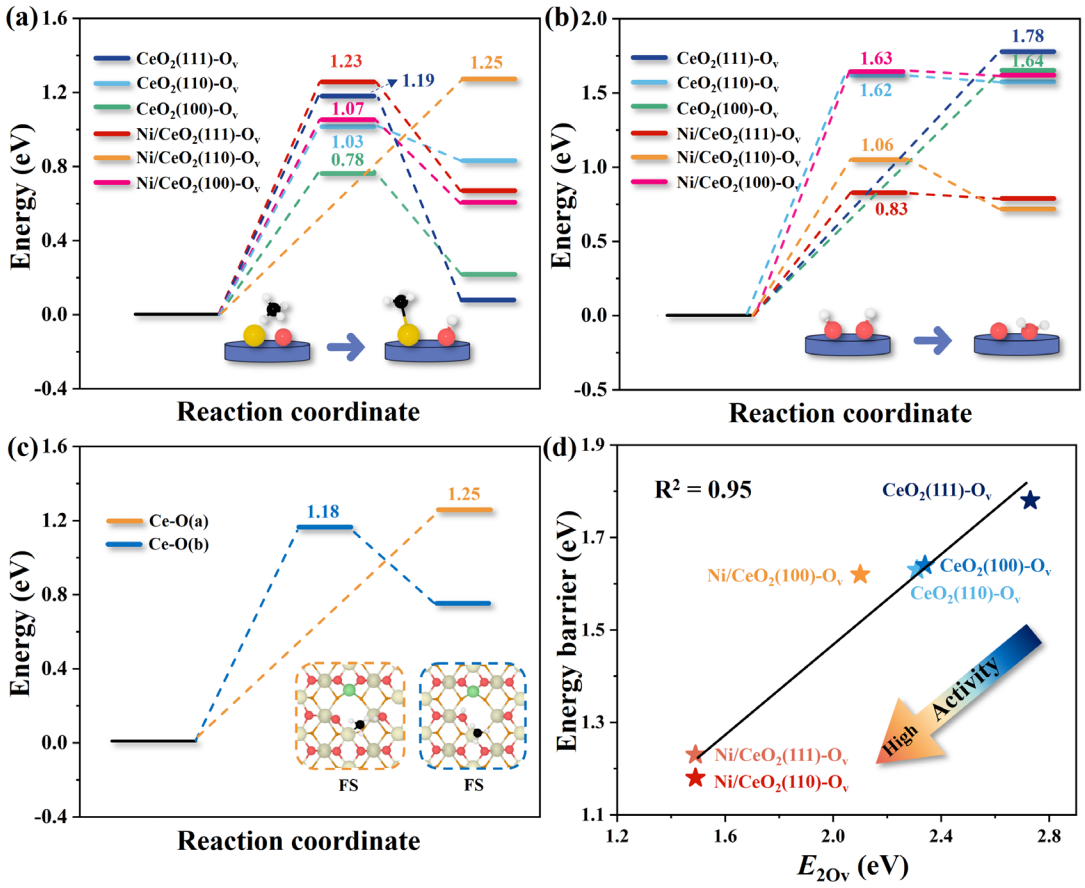


**FIG. 3.** Calculated energetics of (a) $CH_4^* \rightarrow CH_3^* + H^*$ and (b) $2OH^* \rightarrow H_2O^* + O^*$ on the $CeO_2$-$O_v$ and Ni/$CeO_2$-$O_v$ surfaces. (c) Calculated energetics of $CH_4^* \rightarrow CH_3^* + H^*$ on the Ce-O(a) site and Ce-O(b) sites of the Ni/$CeO_2$(110)-$O_v$ surface. (d) Relationship between the highest energy barriers of key steps and the $E_{2Ov}$ values.

Next, we investigated the $H_2O^*$ formation on the $CeO_2$-$O_v$ and Ni/$CeO_2$-$O_v$ surfaces. To determine which O atom is the most easily reduced to $H_2O^*$, we investigated the formation of a new oxygen vacancy on the $CeO_2$-$O_v$ and Ni/$CeO_2$-$O_v$ surfaces and named it as the second oxygen vacancy ($2O_v$) (see Fig. S3). Fig. 1 shows the location for generating the second oxygen vacancy with the lowest energy cost, indicated by the purple dashed circles. The data shown in Table 1 demonstrate that the

second oxygen vacancy ($E_{2Ov}$) on the $CeO_2$ surface follows the same trend as the $E_{Ov}$. The (111) surface has the highest $E_{2Ov}$ of 2.73 eV, while the (110) surface has the lowest $E_{2Ov}$ of 2.31 eV. In contrast, the $E_{2Ov}$ values on the Ni/$CeO_2$ surfaces are markedly smaller. Compared to the pristine $CeO_2$ surface, the trend changes from (111) > (100) > (110) to (100) > (111) = (110). Upon the comparison of the above results, it is observed that on the Ni/$CeO_2$(111) and (110) surfaces, the second oxygen vacancy tends to be generated by the two-coordinated oxygen (O(b)) rather than the oxygen of the FLP site (O(a)). According to Bader analysis, the Bader charges of O(a) and O(b) are –1.19 and –1.05 |e|, respectively. Therefore, compared to O(a), O(b) has less electron transfer with Ce sites, indicating a weaker interaction with the surface. This makes O(b) more reactive as a lattice oxygen (see Figs. 2(b) and 2(d)).

Then, the energetics of $H_2O$* formation on these surfaces were calculated, and the optimized geometries of stationary points along the reaction path are shown in Fig. S4. Table 2 and Fig. 3(b) show that the $H_2O$* formation barriers (or endothermicities in the absence of barriers) on $CeO_2$(111), (110) and (100)-$O_v$ surfaces are 1.78, 1.62 and 1.64 eV, respectively. Interestingly, these values are higher than the corresponding $CH_4$* activation barriers, suggesting that the formation of $H_2O$ on pristine surfaces is more difficult. We further investigated the effect of H coverage on the $H_2O$* formation step as shown in Fig. S5. The results show that on the $CeO_2$(111)-$O_v$ surface, a small amount of H coverage promotes $H_2O$* formation. On the $CeO_2$(110)-$O_v$ and $CeO_2$(100)-$O_v$ surfaces, it is found that the additional H increases the reaction energy of $H_2O$* formation. However, the formation of $H_2O$ is still more difficult than the activation of

$CH_4$* on all three surfaces. Therefore, solely considering $CH_4$* activation as an indicator for evaluating catalytic activity is apparently inadequate and potentially misleading. On Ni-doped $CeO_2$ surfaces, the energy barriers of $H_2O$ formation are reduced to 0.83, 1.06 and 1.63 eV for (111), (110) and (100) facets, respectively, indicating that $H_2O$* formation is easier on Ni/$CeO_2$-$O_v$ surfaces compared to the $CeO_2$-$O_v$ surfaces. It is worth mentioning that the $H_2O$* formation barriers remain higher than $CH_4$* activation on the Ni/$CeO_2$(100)-$O_v$ surface.

To verify if $CH_4$* activation on the Ni/$CeO_2$(111)/(110)-$O_v$ surfaces can occur on O(b) sites, additional calculations on the energy barrier of the C-H bond on the Ce-O(b) site were conducted. However, the distance between Ce-O(b) on the Ni/$CeO_2$(111) surface is too long (6.58 Å) to serve as the site for $CH_4$* dissociation into $CH_3$* and H* (see Fig. 2(b)). In contrast, the Ce-O(b) site on the Ni/$CeO_2$(110)-$O_v$ surface exhibits superior activation of the C-H bond, with a lower barrier than the Ce-O(a) FLP site (1.18 *vs.* 1.25 eV, as shown Fig. 3(c)). This implies that on the Ni/$CeO_2$(110)-$O_v$ surface, the two-coordinated oxygen serves as the primary site for both $CH_4$ activation and $H_2O$ formation.

To further understand the influence of $O_v$ formation on the catalytic activity, the relationship of $E_{2Ov}$ with the highest energy barriers of the key steps is investigated, as displayed in Fig. 3(d). The data shows a linear relationship between the barriers and $E_{2Ov}$, indicating that lower $E_{2Ov}$ values correspond to lower barriers. Given the multiple possibilities revealed by these results, a comprehensive assessment of both $CH_4$* activation and $H_2O$* formation steps seems to be necessary to explain the

experimentally observed positive correlation between the redox properties of $CeO_2$ surfaces and catalytic activity. As shown in Fig. 3(d), the activity is most significantly enhanced on Ni/$CeO_2$(111)/(110)-$O_v$ surfaces due to the formation of active two-coordinated oxygen species upon Ni doping, which enhances surface redox properties. Unlike many other doped metals on $CeO_2$ surfaces that directly participate in the reaction,[52-54] the Ni dopant serves as a single-atom promotor as it is not actively involved in the catalysis.[29, 30] Overall, we have compared the effects of different crystal planes and Ni doping on the key steps of the $CH_4$ oxidation reaction under the same vacancy coverage, but there are some other factors that could be further investigated in the future, such as the oxygen vacancy concentration.

### C. Methane oxidation mechanism on $CeO_2$(110)-$O_v$ and Ni/$CeO_2$(110)-$O_v$

To gain a more complete understanding of the reaction pathways, we studied the entire process of $CH_4$ oxidation on the most promising Ni/$CeO_2$(110)-$O_v$ surface and compared it with the corresponding $CeO_2$(110)-$O_v$ surface. The corresponding geometries, reaction energies ($\Delta E$), and barriers ($E_a$) for elementary steps are shown in Figs. S6-S7 and Table 3. Fig. 4 illustrates the potential energy diagram for the catalytic cycle on the $CeO_2$(110)-$O_v$ and Ni/$CeO_2$(110)-$O_v$ surfaces with illustrations of the stationary point geometries.

**TABLE 3.** Reaction energies ($\Delta E$) and energy barriers ($E_a$) for the elementary steps in $CH_4$ oxidation on $CeO_2$(110)-$O_v$ and Ni/$CeO_2$(110)-$O_v$ surfaces.

| Steps | $CeO_2$(110)-$O_v$ | Ni/$CeO_2$(110)-$O_v$ | Notes |
|---|---|---|---|

| | $\Delta E$ (eV) | $E_a$ (eV) | $\Delta E$ (eV) | $E_a$ (eV) | |
|---|---|---|---|---|---|
| S0 to S1 | –0.61 | – | –0.33 | – | $CH_4$ adsorption |
| S1 to S2 | 0.83 | 1.03 | 0.75 | 1.18 | First C–H bond cleavage |
| S2 to S3 | –0.28 | – | 0.27 | 0.37 | H* migration |
| S3 to S4 | 0.90 | 1.01 | 0.50 | 0.79 | Second C–H bond cleavage |
| S4 to S5 | 1.07 | 1.37 | 0.72 | 1.06 | $H_2O$* formation |
| S5 to S6 | 0.80 | – | 0.95 | – | $H_2O$* desorption |
| S6 to S7 | –1.62 | – | –3.41 | – | $O_2$ adsorption |
| S7 to S8 | –1.49 | 0.28 | – | – | $O_2$--$CH_2$* complex formation |
| S8 to S9 | –2.84 | – | –2.85 | 0.06 | O–O bond cleavage and $CH_2O$* formation |
| S9 to S10 | 0.06 | 0.27 | 0.06 | 0.93 | Third C–H bond cleavage |
| S10 to S11 | –0.35 | – | 0.16 | 0.31 | H* migration |
| S11 to S12 | – | – | 0.68 | – | CHO* transformation |
| S12 to S13 | –1.11 | 0.33 | –2.72 | – | Fourth C–H bond cleavage |
| S13 to S14 | 1.58 | 1.62 | 1.00 | – | $H_2O$* formation |
| S14 to S15 | 0.74 | – | 1.03 | – | $H_2O$* desorption |
| S15 to S16 | –3.05 | – | –1.58 | – | $O_2$ adsorption |
| S16 to S17 | –1.35 | 0.53 | 0.71 | 0.77 | $O_2$--CO* complex formation |
| S17 to S18 | –1.25 | 0.23 | –4.09 | 0.45 | O–O bond cleavage and $CO_2$* formation |
| S18 to S0 | 0.31 | – | 0.48 | – | $CO_2$* desorption |

Note: "–" represents the absence of transition states or corresponding intermediates.

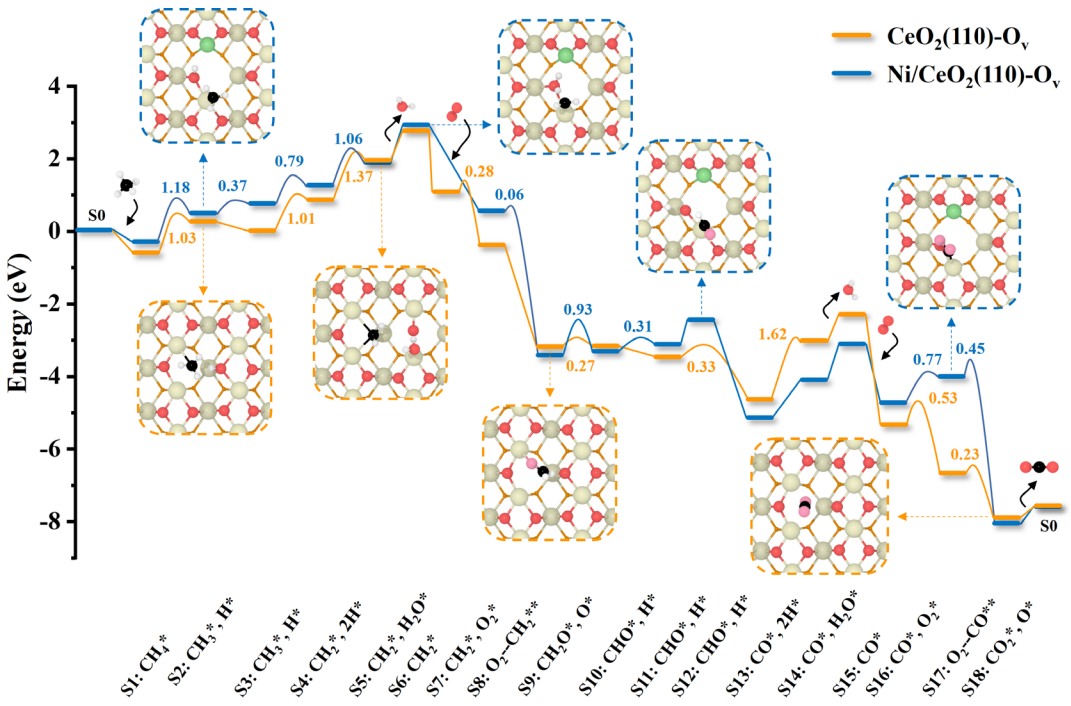


**FIG. 4.** Potential energy diagram for the reaction $CH_4 + 2O_2 \rightarrow 2H_2O + CO_2$ on $CeO_2(110)$-$O_v$ and $Ni/CeO_2(110)$-$O_v$ surfaces. The structures of selected intermediates are illustrated (all structures in Figs. S6 and S7). Color scheme: Ce, yellow; Ni, green; C, black; H, white, surface O, red; subsurface O, orange; O in adsorbate, pink; The adsorbed species are denoted with asterisks (*).

On $Ni/CeO_2(110)$-$O_v$, $CH_4$ is first adsorbed above an oxygen vacancy with an adsorption energy of –0.33 eV, followed by the first C–H bond activation, leading to a $CH_3$* species adsorbed on the Ce site and H* captured by the O(b) (S1 to S2) after overcoming a barrier of 1.18 eV. Since the further dehydrogenation of the $CH_3$* species requires a high barrier of up to 1.68 eV (Fig. S8), the H* species first migrate to the adjacent lattice oxygen with a low barrier of 0.37 eV (S2 to S3) before breaking the second C–H bond, forming $CH_2$* and H* adsorbed on the vacant O(b) site with an

endothermicity of 0.50 eV and a barrier of 0.79 eV (S3 to S4). Next, the migrated H* species returned to the O(b) site through a 1.06 eV barrier, producing the first $H_2O$* and $CH_2$* co-adsorbed on the Ni/$CeO_2$(110)-$O_v$ surface (S4 to S5).

Likewise, the further activation of the third C–H bond before forming the first $H_2O$* is also an unfavorable step compared to $H_2O$* formation (Fig. S9). Desorption of the product $H_2O$* leaves an oxygen vacancy on the surface (S6). Next, an $O_2$ molecule fills this vacancy and spontaneously forms the $O_2$--$CH_2$** complex by attacking $CH_2$* (S8). After that, the O–O bond in $O_2$--$CH_2$** breaks, releasing 2.85 eV of energy. One O atom restores the oxygen vacancy, and $CH_2O$* remains adsorbed on the Ce site (S8 to S9). The activation of the third C–H bond is slightly endothermic. After overcoming a 0.93 eV barrier, O(b) captures the H atom, forming CHO* (S9 to S10).

The fourth C–H bond undergoes barrierless activation (S10 to S13) through H* migration and CHO* transformation, resulting in the oxidation of $CH_4$* to CO*. Similarly, the migrating H* returns to the O(b) site and combines with the hydroxyl group, producing the second $H_2O$*. This step has no transition state but an endothermicity of 1.00 eV (S13 to S14). The resulting $H_2O$* species desorbs, creating an oxygen vacancy to accommodate the adsorption of the second $O_2$ (S15). Upon $O_2$ adsorption, the O–O bond is activated with an adsorption energy of –1.58 eV (S16). The combination of co-adsorbed $O_2$* and CO* leads to the formation of $O_2$--CO** complex, which requires an endothermicity of 0.71 eV and a barrier of 0.77 eV (S16 to S17). Finally, the $O_2$--CO* undergoes further O–O bond cleavage, restoring the oxygen vacancy and yielding the final oxidized product $CO_2$* (S17 to S18). Meanwhile, we

also explored the mechanism starting from $O_2$ adsorption, as shown in Fig. S10 and Table S3. $O_2$ tends to adsorb on the Ce site of the Ni/$CeO_2$(110)-$O_v$ surface, yielding an adsorption energy of –0.47 eV. However, the subsequent dissociation of $O_2$* into two O* atoms is highly endothermic up to 2.86 eV, thus hindering the reaction progress and is not considered further. Overall, the rate-determining step of the entire reaction cycle is the activation of $CH_4$*, where O(b) plays a crucial role in trapping the H* species and participating in the reduction to $H_2O$*.

On the $CeO_2$(110)-$O_v$ surface, $CH_4$ adsorption is stronger than that on Ni/$CeO_2$(110)-$O_v$ with a calculated adsorption energy of –0.61 eV. The first chemical step involves $CH_4$* dissociation into $CH_3$* and H* at the Ce-O(a) FLP site by overcoming an energy barrier of 1.03 eV. Subsequently, the resulting $CH_3$* undergoes continuous dehydrogenation and oxidation to $CO_2$* through a similar pathway as on Ni/$CeO_2$(110)-$O_v$. Compared to the Ni/$CeO_2$(110)-$O_v$ surface, the $CeO_2$(110)-$O_v$ surface has a lower barrier for $CH_4$* dissociation but a higher barrier for the subsequent $H_2O$* formation, which is the rate-determining step in the overall reaction pathway due to the more stabilized lattice oxygen. The energy barrier for the second $H_2O$* formation is 1.62 eV. In fact, at the beginning of the reaction, the active site is likely to be blocked and the reaction may be hindered due to the strong competition between $O_2$ and $CH_4$ adsorption on the $CeO_2$(110)-$O_v$ surface and the difficulty of dissociating $O_2$* into active oxygen with a reaction energy of 1.76 eV (Fig. S11 and Table S3).

The above results suggest that $CH_4$ oxidation on the $CeO_2$(110)-$O_v$ and Ni/$CeO_2$(110)-$O_v$ catalysts proceeds via the Mars-van Krevelen (MvK) mechanism,

which is typical for metal oxide catalysts. For example, Chen et al. proposed that $CH_4$ oxidation on $Ni_{10}/CeO_2(111)$ catalysts proceeds through $CH_4$* activation at the Ni-$CeO_2$ interface, followed by $CH_4$* dissociation and $H_2O$* formation.[28] The calculated heats of reaction for these steps are about 1.10 and 2.00 eV, respectively. The reaction eventually oxidizes to $CO_2$ and $H_2O$ via the MvK mechanism.[28] The major difference of our model from that of Chen et al. is that Ni in our models is a dopant while the previous work studied a Ni cluster adsorbed on the $CeO_2$ surface.

In short, based on this work and some earlier studies[27, 28] of the $CH_4$ oxidation mechanism, both $CH_4$* activation and $H_2O$* formation are shown to be the key catalytic steps. As an atomic dopant, Ni regulates the surface properties and balances the kinetics of $CH_4$* activation and $H_2O$* formation, leading to a shift in the rate-determining step and an improvement in overall reactivity of $CeO_2$ catalysts.

## IV. Microkinetic simulations

Microkinetic simulations facilitate our understanding of the overall reaction mechanism of complex reactions under realistic conditions. To further elucidate the activity of catalyzed $CH_4$ oxidation under different working conditions and to quantify the contribution of the elementary reaction steps, we performed microkinetic simulations based on the energetics of all of the aforementioned elementary reaction steps.

The turnover frequencies (TOF) of $CO_2$ products calculated on the $CeO_2(110)$-$O_v$ and $Ni/CeO_2(110)$-$O_v$ catalysts at a temperature range of 400 to 1000 K and a pressure

range of 0.01 to 1 bar are displayed in Figs. 5(a) and 5(b). The results show that the TOF for $CO_2$ production varies significantly with temperature, while only at medium-high temperatures a weak variation with pressure was observed. This is apparently due to the significant effect that small molecules have on the entropy value at medium and high temperatures. Moreover, the Ni/$CeO_2$(110)-$O_v$ catalyst exhibits 3-4 orders of magnitude higher TOFs of $CO_2$ production than the $CeO_2$(110)-$O_v$ catalyst at all temperature and pressure ranges. Specifically, the TOF of $CO_2$ formation on Ni/$CeO_2$(110)-$O_v$ at 900 K and a total pressure of 1 bar can reach $5.83\times10^{-3}$ $s^{-1}$, compared to $2.75\times10^{-6}$ $s^{-1}$ on the $CeO_2$(110)-$O_v$ catalyst. This difference is consistent with the DFT barriers. Furthermore, changing the ratio of $CH_4$:$O_2$ has a minor effect on the TOFs of $CO_2$ production (see Figs. S12 and S13). Unfortunately, there is still no report on measurements of TOF on these catalysts.

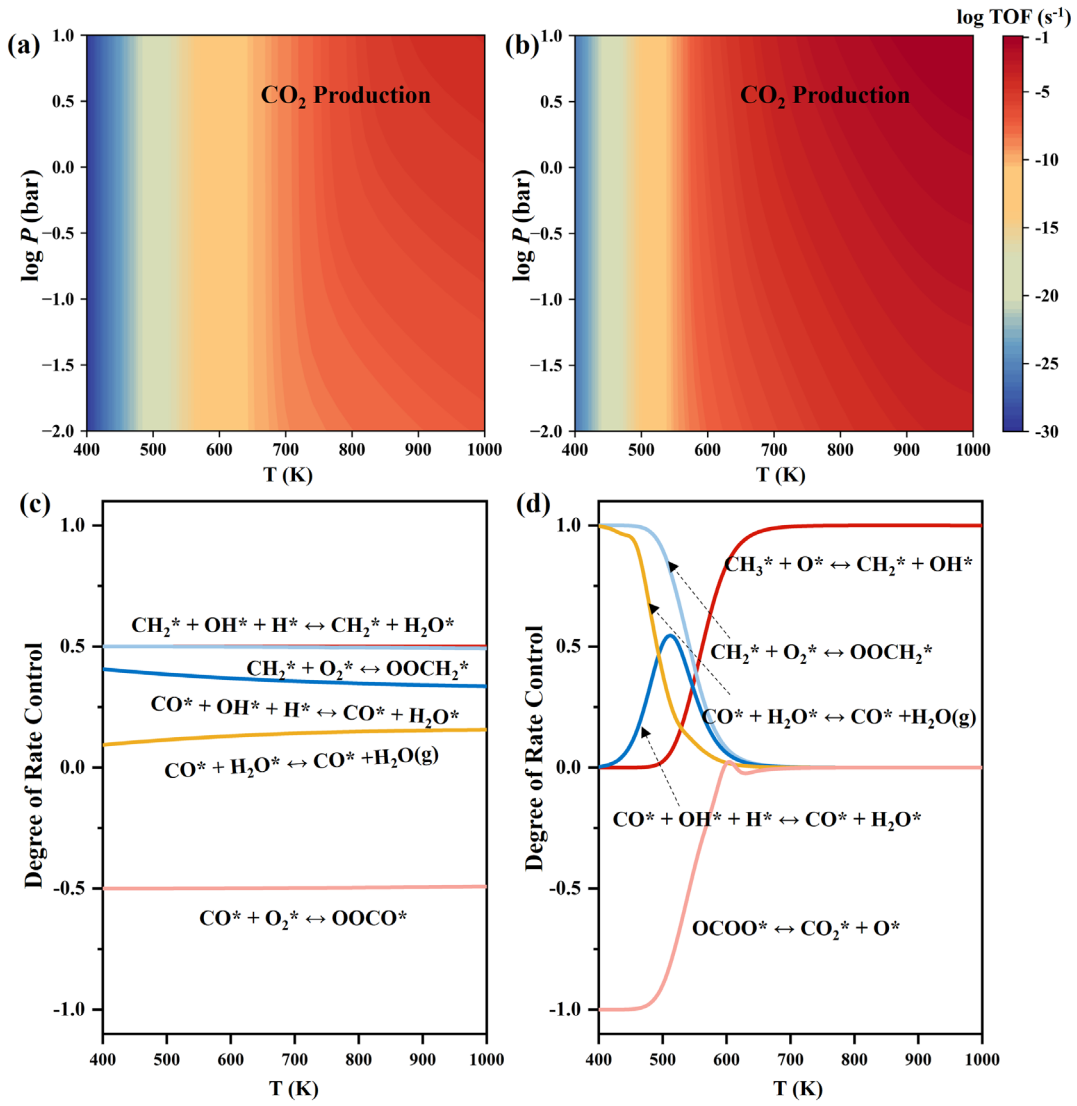


**FIG. 5.** Map of TOF under different pressure (P) and temperature (T) working conditions for the $CH_4$ oxidation reaction on the (a) $CeO_2(110)$-$O_v$ and (b) Ni /$CeO_2(110)$-$O_v$ surfaces for $CO_2$ production. Degree of rate control analysis as a function of temperature on (c) $CeO_2(110)$-$O_v$ and (d) Ni/$CeO_2(110)$-$O_v$ surfaces.

The degree of rate control (DRC) reflects the sensitivity of elementary steps throughout the entire reaction.[55] As shown in Fig. 5(c), DRC analysis indicates that reducing the $H_2O$* formation barrier and accelerating the coupling of $CH_2$* with $O_2$* are crucial for enhancing the overall reaction rate on the $CeO_2(110)$-$O_v$ catalyst. This is

because the high energy barrier of the former limits the reaction rate, while the latter promotes the consumption of $CH_2$* species facilitating the reaction in a positive direction. For the Ni/$CeO_2$(110)-$O_v$ catalyst, DRC analysis revealed that the generation and desorption of $H_2O$* and the coupling of $CH_2$* to $O_2$* were important steps affecting the overall reaction rate only at low temperatures, but became irrelevant above 600 K (Fig. 5(d)). This is attributed to the reduced energy barrier for $H_2O$* formation on the Ni/$CeO_2$(110)-$O_v$ catalyst, which becomes less challenging after 600 K. Under these circumstances, the formation of OH* species makes the largest contribution to the overall reaction rate. These results indicate that Ni-doped $CeO_2$(110) significantly enhances the activation of catalytic $CH_4$ oxidation under simulated conditions, consistent with the recent experimental observations [18]. This provides useful insights for designing low-temperature $CH_4$ oxidation catalysts.

## V. Conclusions

In summary, we performed a comprehensive assessment of the key steps of $CH_4$ oxidation and their dependence on surface properties in pristine and Ni-doped $CeO_2$ surfaces using DFT. Several models, including $CeO_2$(111), $CeO_2$(110), $CeO_2$(100), Ni/$CeO_2$(111), Ni/$CeO_2$(110) and Ni/$CeO_2$(100) containning one $O_v$, have been constructed to understand the impact of the redox properties on the catalysis. The $CH_4$ oxidation activity and reaction mechanism on $CeO_2$(110)-$O_v$ and Ni/$CeO_2$(110)-$O_v$ were explored further using microkinetic simulations. The main conclusions are as follows: (1) The ease of oxygen vacancy formation ($E_{Ov}$ ) for the pristine $CeO_2$ surface ranks as (111) > (100) > (110). However, the Ni doping generates two-coordinated

oxygen on the (111) and (110) surfaces, and oxygen vacancies are formed spontaneously. As a result, the order of $E_{Ov}$ changes to (100) > (111) = (110). (2) The highest energy barriers for $CH_4$* activation and $H_2O$* formation on the $CeO_2$-$O_v$ and Ni/$CeO_2$-$O_v$ surfaces are linearly correlated with $E_{2Ov}$, with the Ni/$CeO_2$-$O_v$(110) surface possessing the best activity for $CH_4$ oxidation. (3) The $CH_4$ oxidation reaction on $CeO_2$(110)-$O_v$ and Ni/$CeO_2$(110)-$O_v$ surfaces follows the MvK mechanism. With Ni doping, the rate-determining step shifts from $CH_4$* activation to $H_2O$* formation. The energy barrier of the rate-determining step decreases from 1.62 to 1.18 eV upon Ni doping, which significantly improves the overall activity of the $CeO_2$ catalyst. (4) Microkinetic simulations demonstrate that the TOFs values of $CO_2$ conversion on Ni/$CeO_2$-$O_v$(110) are 3-4 orders of magnitude higher than those of $CeO_2$-$O_v$(110), which rationalizes the experimental observation of the superior performance of Ni-doped $CeO_2$ catalysis of $CH_4$ oxidation. Finally, it is concluded that the formation of $H_2O$* as an elementary step significantly contributes to the overall reaction rate. These insights help to shed light on the mechanisms of $CH_4$ oxidation catalyzed by metal oxide catalysts.

## ASSOCIATED CONTENT

**Supporting Information:** Additional results.

## Notes

The authors declare no competing financial interests.

## Acknowledgments

We thank the National Natural Science Foundation of China (22373017 to S.L., 2196020126 to S.Z. and 22303085 to Q.W.) and the “Chuying Program” for the Top Young Talents of Fujian Province (S.L.). H.G. is funded by the US National Science Foundation (Grant number CHE-2306975). Computations were performed at the Hefei Advanced Computing Center and Supercomputing Center of Fujian. We thank Prof. Abhaya Datye for several useful discussions.

## REFERENCES

[1] P. Da, L. Tao, K. Sun, L.M. Golston, D.J. Miller, T. Zhu, Y. Qin, Y. Zhang, D.L. Mauzerall, M.A. Zondlo, "Methane Emissions from Natural Gas Vehicles in China," Nat. Commun. **11**, 4588 (2020).

[2] D. Jiang, K. Khivantsev, Y. Wang, "Low-Temperature Methane Oxidation for Efficient Emission Control in Natural Gas Vehicles: Pd and Beyond," ACS Catal. **10**, 14304-14314 (2020).

[3] R.J. Farrauto, "Low-Temperature Oxidation of Methane," Science **337**, 659-660 (2012).

[4] J. Yang, M. Peng, G. Ren, H. Qi, X. Zhou, J. Xu, F. Deng, Z. Chen, J. Zhang, K. Liu, X. Pan, W. Liu, Y. Su, W. Li, B. Qiao, D. Ma, T. Zhang, "A Hydrothermally Stable Irreducible Oxide-Modified Pd/$MgAl_2O_4$ Catalyst for Methane Combustion," Angew. Chem. Int. Ed. **59**, 18522-18526 (2020).

[5] M. Cargnello, J.J.D. Jaén, J.C.H. Garrido, K. Bakhmutsky, T. Montini, J.J.C. Gámez, R.J. Gorte, P. Fornasiero, "Exceptional Activity for Methane Combustion over Modular Pd@$CeO_2$ Subunits on Functionalized $Al_2O_3$," Science **337**, 713-717 (2012).

[6] P. Tang, Q. Zhu, Z. Wu, D. Ma, "Methane Activation: the Past and Future," Energy Environ. Sci. **7**, 2580-2591 (2014).

[7] H. Xiong, D. Kunwar, D. Jiang, C.E. García-Vargas, H. Li, C. Du, G. Canning, X.I. Pereira-Hernandez, Q. Wan, S. Lin, S.C. Purdy, J.T. Miller, K. Leung, S.S. Chou, H.H. Brongersma, R. ter Veen, J. Huang, H. Guo, Y. Wang, A.K. Datye, "Engineering Catalyst Supports to Stabilize $PdO_x$ Two-dimensional Rafts for Water-tolerant Methane Oxidation," Nat. Catal. **4**, 830-839 (2021).

[8] Q. Wan, V. Fung, S. Lin, Z. Wu, D.-e. Jiang, "Perovskite-supported Pt Single Atoms for Methane Activation," J. Mater. Chem. A **8**, 4362-4368 (2020).

[9] Q. Huang, W. Li, Q. Lin, X. Zheng, H. Pan, D. Pi, C. Shao, C. Hu, H. Zhang, "Catalytic Performance of Pd–$NiCo_2O_4$/$SiO_2$ in Lean Methane Combustion at Low Temperature," J. Energy Inst. **91**, 733-742 (2018).

[10] T. Montini, M. Melchionna, M. Monai, P. Fornasiero, "Fundamentals and Catalytic Applications of $CeO_2$-Based Materials," Chem. Rev. **116**, 5987-6041 (2016).

[11] X. Zhang, S.D. House, Y. Tang, L. Nguyen, Y. Li, A.A. Opalade, J.C. Yang, Z. Sun, F.F. Tao, "Complete Oxidation of Methane on NiO Nanoclusters Supported on $CeO_2$ Nanorods through Synergistic Effect," ACS Sustainable Chem. Eng. **6**, 6467-6477 (2018).

[12] Z. Wu, M. Li, S.H. Overbury, "On the Structure Dependence of CO Oxidation over $CeO_2$ Nanocrystals with Well-defined Surface Planes," J. Catal. **285**, 61-73 (2012).

[13] Z. Zhou, L. Chen, L. Wang, Y. Liu, P. Cheng, H. Peng, J. Cai, Q. Zhou, Y. Wang, N. Yang, B. Wang, X.-Q. Gong, F. Yang, Z. Liu, "Selective Hydrogenation of Propyne to Propene Promoted by Synergistic Effect of Surface Oxygen Vacancies and Hydride Species on Ceria," ACS Catal. **13**, 9588-9596 (2023).

[14] X.-P. Wu, X.-Q. Gong, "Unique Electronic and Structural Effects in Vanadia/Ceria-Catalyzed Reactions," J. Am. Chem. Soc. **137**, 13228-13231 (2015).

[15] Y. Lu, C. Thompson, D. Kunwar, A.K. Datye, A.M. Karim, "Origin of the High CO Oxidation Activity on $CeO_2$ Supported Pt Nanoparticles: Weaker Binding of CO or Facile Oxygen Transfer from the Support?," ChemCatChem **12**, 1726-1733 (2020).

[16] J. Paier, C. Penschke, J. Sauer, "Oxygen Defects and Surface Chemistry of Ceria: Quantum Chemical Studies Compared to Experiment," Chem. Rev. **113**, 3949-3985 (2013).

[17] Y.-Q. Su, J.-X. Liu, I.A.W. Filot, L. Zhang, E.J.M. Hensen, "Highly Active and Stable $CH_4$ Oxidation by Substitution of $Ce^{4+}$ by Two $Pd^{2+}$ Ions in $CeO_2(111)$," ACS Catal. **8**, 6552-6559 (2018).

[18] J. Chen, H.N. Pham, T. Mon, T.J. Toops, A.K. Datye, Z. Li, E.A. Kyriakidou, "Ni/$CeO_2$ Nanocatalysts with Optimized $CeO_2$ Support Morphologies for $CH_4$ Oxidation," ACS Appl. Nano Mater. **6**, 4544-4553 (2023).

[19] J.H. Lee, D.Y. Jo, J.W. Choung, C.H. Kim, H.C. Ham, K.-Y. Lee, "Roles of noble metals (M = Ag, Au, Pd, Pt and Rh) on $CeO_2$ in enhancing activity toward soot oxidation: Active oxygen species and DFT calculations," J. Hazard. Mater. **403**, 124085 (2021).

[20] T. Ban, X.-Y. Yu, H.-Z. Kang, Z.-Q. Huang, J. Li, C.-R. Chang, "Design of SA-FLP Dual Active Sites for Nonoxidative Coupling of Methane," ACS Catal. **13**, 1299-1309 (2023).

[21] S.D. Senanayake, J.A. Rodriguez, J.F. Weaver, "Low Temperature Activation of Methane on Metal-Oxides and Complex Interfaces: Insights from Surface Science," Acc. Chem. Res. **53**, 1488-1497 (2020).

[22] G. Kumar, S.L.J. Lau, M.D. Krcha, M.J. Janik, "Correlation of Methane Activation and Oxide Catalyst Reducibility and Its Implications for Oxidative Coupling," ACS Catal. **6**, 1812-1821 (2016).

[23] P.G. Lustemberg, P.J. Ramírez, Z. Liu, R.A. Gutiérrez, D.G. Grinter, J. Carrasco, S.D. Senanayake, J.A. Rodriguez, M.V. Ganduglia-Pirovano, "Room-Temperature Activation of Methane and Dry Re-forming with $CO_2$ on Ni-$CeO_2$(111) Surfaces: Effect of $Ce^{3+}$ Sites and Metal–Support Interactions on C–H Bond Cleavage," ACS Catal. **6**, 8184-8191 (2016).

[24] H. Zhu, Y. Hou, H. Ren, D. Liu, X. Li, L. Zhao, Y. Chi, W. Guo, "Theoretical Investigation on $H_2$ Oxidation Mechanisms over Pristine and Sm-doped $CeO_2$(111) Surfaces," Appl. Surf. Sci. **511**, 145388 (2020).

[25] M. Jing, W. Song, L. Chen, S. Ma, J. Deng, H. Zheng, Y. Li, J. Liu, Z. Zhao, "Density Functional Theory Study of the Formaldehyde Catalytic Oxidation Mechanism on a Au-Doped $CeO_2$(111) Surface," J. Phys. Chem. C **122**, 438-448 (2018).

[26] Y. Choi, H. Ha, J. Kim, H.G. Seo, H. Choi, B. Jeong, J. Yoo, E.J. Crumlin, G. Henkelman, H.Y. Kim, W. Jung, "Unveiling Direct Electrochemical Oxidation of Methane at the Ceria/Gas Interface," Adv. Mater, 2403626 (2024).

[27] Q. Wan, H. Li, S. Liu, Z. Zhang, H. Xiong, S. Lin, "Investigation on the Reaction Mechanism of Methane Oxidation over $MgAl_2O_4$-Supported Single-Atom Catalyst Prepared at High Temperature," ChemCatChem **14**, e202200919 (2022).

[28] J. Chen, T. Buchanan, E.A. Walker, T.J. Toops, Z. Li, P. Kunal, E.A. Kyriakidou, "Mechanistic Understanding of Methane Combustion over Ni/$CeO_2$: A Combined Experimental and Theoretical Approach," ACS Catal. **11**, 9345-9354 (2021).

[29] C. Riley, S. Zhou, D. Kunwar, A. De La Riva, E. Peterson, R. Payne, L. Gao, S. Lin, H. Guo, A. Datye, "Design of Effective Catalysts for Selective Alkyne Hydrogenation by Doping of Ceria with a Single-Atom Promotor," J. Am. Chem. Soc. **140**, 12964-12973 (2018).

[30] S. Zhou, Q. Wan, S. Lin, H. Guo, "Acetylene hydrogenation catalyzed by bare and Ni doped $CeO_2$(110): the role of frustrated Lewis pairs," Phys. Chem. Chem. Phys. **24**, 11295-11304 (2022).

[31] G. Kresse, J. Furthmüller, "Efficient Iterative Schemes for Ab Initio Total-energy Calculations Using a Plane-wave Basis Set," Phys. Rev. B **54**, 11169-11186 (1996).

[32] G. Kresse, J. Furthmüller, "Efficiency of Ab-initio Total Energy Calculations for Metals and Semiconductors Using a Plane-wave Basis Set," Comput. Mater. Sci. **6**, 15-50 (1996).

[33] P.E. Blöchl, "Projector Augmented-wave Method," Phys. Rev. B **50**, 17953-17979 (1994).

[34] S. Grimme, J. Antony, S. Ehrlich, H. Krieg, "A Consistent and Accurate Ab Initio Parametrization of Density Functional Dispersion Correction (DFT-D) for the 94 Elements H-Pu," J. Chem. Phys. **132**, 154104 (2010).

[35] J.P. Perdew, K. Burke, M. Ernzerhof, "Generalized Gradient Approximation Made Simple," Phys. Rev. Lett. **77**, 3865-3868 (1996).

[36] M.D. Krcha, M.J. Janik, "Challenges in the Use of Density Functional Theory to Examine Catalysis by M-doped Ceria Surfaces," Int. J. Quantum Chem. **114**, 8-13 (2014).

[37] H.J. Monkhorst, J.D. Pack, "Special Points for Brillouin-zone Integrations," Phys. Rev. B **13**, 5188-5192 (1976).

[38] G. Henkelman, B.P. Uberuaga, H. Jónsson, "A Climbing Image Nudged Elastic Band Method for Finding Saddle Points and Minimum Energy Paths," J. Chem. Phys. **113**, 9901-9904 (2000).

[39] G. Henkelman, H. Jónsson, "A Dimer Method for Finding Saddle Points on High Dimensional Potential Surfaces Using Only First Derivatives," J. Chem. Phys. **111**, 7010-7022 (1999).

[40] J. Chen, M. Jia, P. Hu, H. Wang, "CATKINAS: A Large-scale Catalytic Microkinetic Analysis Software for Mechanism Auto-analysis and Catalyst Screening," J. Comput. Chem. **42**, 379-391 (2021).

[41] J.-F. Chen, Y. Mao, H.-F. Wang, P. Hu, "Reversibility Iteration Method for Understanding Reaction Networks and for Solving Microkinetics in Heterogeneous Catalysis," ACS Catal. **6**, 7078-7087 (2016).

[42] E.A. Kümmerle, G. Heger, "The Structures of C–$Ce_2O_3^{+\delta}$, $Ce_7O_{12}$, and $Ce_{11}O_{20}$," J. Solid State Chem. **147**, 485-500 (1999).

[43] M. Capdevila-Cortada, N. López, "Entropic contributions enhance polarity compensation for $CeO_2$(100) surfaces," Nat. Mater **16**, 328-334 (2017).

[44] Z.-Q. Huang, L.-P. Liu, S. Qi, S. Zhang, Y. Qu, C.-R. Chang, "Understanding All-Solid Frustrated-Lewis-Pair Sites on $CeO_2$ from Theoretical Perspectives," ACS Catal. **8**, 546-554 (2018).

[45] S.-H. Zhong, G. Lu, X.-Q. Gong, "A DFT+U study of the structures and reactivities of polar CeO2(100) surfaces," Chin. J. Catal. **38**, 1138-1147 (2017).

[46] T. Wu, N. López, T. Vegge, H.A. Hansen, "Facet-dependent Electrocatalytic Water Splitting Reaction on $CeO_2$: A DFT + U Study," J. Catal. **388**, 1-10 (2020).

[47] F. Zhang, R.A. Gutiérrez, P.G. Lustemberg, Z. Liu, N. Rui, T. Wu, P.J. Ramírez, W. Xu, H. Idriss, M.V. Ganduglia-Pirovano, S.D. Senanayake, J.A. Rodriguez, "Metal–Support Interactions and C1 Chemistry: Transforming Pt-$CeO_2$ into a Highly Active and Stable Catalyst for the Conversion of Carbon Dioxide and Methane," ACS Catal. **11**, 1613-1623 (2021).

[48] C. Chu, Y. Zhao, S. Li, Y. Sun, "Correlation Between the Acid–base Properties of the $La_2O_3$ Catalyst and its Methane Reactivity," Phys. Chem. Chem. Phys. **18**, 16509-16517 (2016).

[49] D.W. Stephan, G. Erker, "Frustrated Lewis Pair Chemistry: Development and Perspectives," Angew. Chem. Int. Ed. **54**, 6400-6441 (2015).

[50] Q. Wan, S. Lin, H. Guo, "Frustrated Lewis Pairs in Heterogeneous Catalysis: Theoretical Insights," Molecules **54**, 3734 (2022).

[51] F. Wei, B. Ge, P. Dong, Q. Wan, X. Hu, S. Lin, "Uncovering the Active Sites of Single Atom-doped Rutile Oxides during Methane Activation by Data-driven Approach," Sci. China Mater. **67**, 1231-1242 (2024).

[52] L. Nie, D. Mei, H. Xiong, B. Peng, Z. Ren, X.I.P. Hernandez, A. DeLaRiva, M. Wang, M.H. Engelhard, L. Kovarik, A.K. Datye, Y. Wang, "Activation of Surface Lattice Oxygen in Single-atom Pt/$CeO_2$ for Low-temperature CO Oxidation," Science **358**, 1419-1423 (2017).

[53] G. Spezzati, Y. Su, J.P. Hofmann, A.D. Benavidez, A.T. DeLaRiva, J. McCabe, A.K. Datye, E.J.M. Hensen, "Atomically Dispersed Pd–O Species on $CeO_2$(111) as Highly Active Sites for Low-Temperature CO Oxidation," ACS Catal. **7**, 6887-6891 (2017).

[54] Y. Lu, S. Zhou, C.-T. Kuo, D. Kunwar, C. Thompson, A.S. Hoffman, A. Boubnov, S. Lin, A.K. Datye, H. Guo, A.M. Karim, "Unraveling the Intermediate Reaction Complexes and Critical Role of Support-Derived Oxygen Atoms in CO Oxidation on Single-Atom Pt/$CeO_2$," ACS Catal. **11**, 8701-8715 (2021).

[55] C.T. Campbell, "The Degree of Rate Control: A Powerful Tool for Catalysis Research," ACS Catal. **7**, 2770-2779 (2017).